Elaboration of a neural-network interatomic potential for silica glass and melt

Salomé Trillot, Julien Lam, Simona Ispas, Akshay Krishna Ammothum
Kandy, Mark Tuckerman, Nathalie Tarrat, Magali Benoit

Elaboration of a neural-network interatomic potential for silica glass and melt

Salomé Trillot[a], Julien Lam[a], Simona Ispas[b], Akshay Krishna Ammothum Kandy[a], Mark E. Tuckerman[c,d,e,f,g], Nathalie Tarrat[a], Magali Benoit[a]

[a]*CEMES-CNRS and Université de Toulouse, 29 Rue Jeanne Marvig, Toulouse, 31055, France*
[b]*Laboratoire Charles Coulomb (L2C), University of Montpellier and CNRS, Place E. Bataillon, 34095, Montpellier, France*
[c]*Department of Physics, New York University, 726 Broadway, New York, New York, 10003, USA*
[d]*Department of Chemistry, New York University (NYU), New York, New York, 10003, USA*
[e]*Courant Institute of Mathematical Sciences, New York University (NYU), New York, New York, 10012, USA*
[f]*NYU-ECNU Center for Computational Chemistry at NYU Shanghai, 3663 Zhongshan Road North, Shanghai, 200062, China*
[g]*Simons Center for Computational Physical Chemistry at New York University, New York, New York, 10003, USA*

Abstract

Because of its importance in various aspects of everyday life, silica is a material that has been the subject of extensive research. Studies on its amorphous phase have particularly benefited from the contribution of atomistic simulations to understand the close relationships between its structure and properties. In this context, the main difficulty lies in the compromise that had to be made between the precision of the interactions that need to be computed at an *ab initio* level and the important statistics required to describe disorder. With the advent of machine learning approaches, it is now possible to couple accuracy and statistics by using interatomic potentials trained on *ab initio* databases. This opens up unprecedented prospects for studies where calculation accuracy, system size and trajectory length are critical. In this work, we propose a machine learning potential for silica obtained from a neural network trained on a database consisting of a few hundred configurations extracted from an *ab initio* molecular dynamics trajectory at the Density Functional Theory (DFT) level of a silica liquid at high temperature and under pressure. We show that this potential is sufficiently accurate to describe the liquid and amorphous phases of silica, and that it is also transferable to glasses under moderate pressure and, more surprisingly, to certain crystalline phases.

Keywords: Liquids; glasses; machine learning; molecular dynamics; neural network; silica.

1. Introduction

Silica is a material that can be found in various aspects of daily life, including window glass and electronic devices, but is also a major component of the glass utilized for nuclear waste storage [1] and of zeolites which are of paramount interest for catalysis and storage [2]. It also plays a fundamental role in the composition of volcanic magmas [3]. The phase diagram of silica is notably extensive, featuring numerous crystalline structures, most of them being composed of tetrahedrally coordinated Si atoms as building blocks [4].

Due to its importance, extensive research has been conducted on silica, particularly in its amorphous state, to gain a deeper understanding of the intricate relationships between its complex and disordered structure and its properties. Numerous atomistic-level numerical studies have specifically focused on these aspects [5–7]. However, this task is made difficult due to the complexity of the phase diagram and to the representation of the amorphous state. In the latter case, because of the structural disorder, previous studies either provided high accuracy in energy description (*ab initio*) but lacked statistical representation [5, 8–12], or offered statistical representation but lacked accuracy[13–17].

Nevertheless, over the past two decades, efforts have been dedicated to developing new interatomic potentials by fitting *ab initio* data, able to properly describe the different phases of silica [18–21]. These advancements have resulted in an increasingly accurate depiction of silica's microscopic properties and hence enabling a better understanding of mechanisms responsible for its behavior during indentation, fracture, varying temperature or pressure [22–26]. Furthermore, the precise derivation of a potential for silica marks the first stage in the development of potentials for silicates incorporating other elements, bringing us closer to modelling increasingly realistic glasses [27–30]. However, despite these significant progresses, these potentials still possess several limitations, particularly in their ability to accurately describe vibrational modes, among other factors [15, 19, 27, 31].

In the pursuit of more accurate potentials, the emergence of machine learning techniques presents an opportunity to take a significant leap forward. Several attempts can be found in the literature, each of which has yielded highly promising results in this regard. In Ref. [31], the authors have used a database made of PBE-DFT calculations of crystalline polymorphs and of snapshots of amorphous samples at several temperatures yielding to a total of 39390 configurations (867 986 atomic environments). After a thorough analysis of the descriptors space, they trained a nonlinear model consisting in 3 layers of 10, 20, 30 or 40 neurons. The obtained root mean square error (RMSE) for the forces lies between 0.38 and 0.22 eV/ Å depending on their parameters. The interaction potential is tested on structure and vibrations of amorphous silica samples and gives good comparison with density functional theory (DFT) calculations. In 2020, Balyakin et al. [32] proposed an interaction potential for silica gener-

2

ated using the DeepMD-kit package [33] with 3 neural networks (NN), two made of 3 layers for the angular and radial filters and one made of 3 layers for the fitting. The database was constructed using 2 sets of *ab initio* molecular dynamics (AIMD) trajectories carried out in the PBE-DFT framework at several temperatures: a 96-atom one and a 216-atom one, yielding to a total of 380 000 configurations (more than 40 millions atomic environments). No RMSE was given. The authors demonstrated the ability of the potential to reproduce the structural and dynamical properties of liquid silica with respect to DFT. More recently, the study presented in [34] focused on a potential trained using the GAP procedure on a DFT database originally obtained with the PBEsol functional then refined with the SCAN one. The configurations were obtained from single-point DFT calculations on snapshots extracted from classical MD simulations using empirical potentials. Besides liquids and amorphous structures, the database also comprised crystalline structures at equilibrium and under strain and small clusters, yielding to a total of 3074 configurations. The RMSE were of the order of 0.01 eV/atom for the energies and of 0.3 eV/Å for the forces in the liquid state, less for crystals. The interatomic potential was able to well reproduce the elastic properties of the crystals and the phonon bands of α-quartz, as well as the pressure-density evolution in SiO_2 glasses up to 40 GPa. However no information were provided about the vibrations in the glass. In 2023, Qi *et al.* [35] published a NN potential obtained also with DeepMD-kit using two 3-layers NN, one

for the descriptors (3 layers of 25, 50 and 100 neurons) and one for the fitting (3 layers of 240 neurons each). The NN was fitted on energies, forces and stress extracted from AIMD simulations of silica glass carried out at 300K and 1000K using two different exchange and correlations functionals, PBE and AM05 with Grimme dispersion corrections. The results show good structural properties of silica glass at ambient pressure but the systems behave strangely under pressure with a very high proportion of 5-fold coordinated Si atoms from 8 GPa and important finite size effects.

In this context, we present a simple protocol for developing a robust and precise machine learning model using a moderately sized database consisting exclusively of high-temperature and compressed liquid configurations. We demonstrate that a compact neural network can effectively generate accurate machine learning potentials when trained on a reduced database consisting of DFT energies and forces of snapshots extracted from MD trajectories at high temperature and pressure, allowing for an extensive exploration of the potential energy landscape. Once validated, the potential is initially employed to investigate the effects of simulation conditions, such as quench rate and system size, on the structural and dynamic properties of amorphous silica. Subsequently, the transferability of the model is tested on silica crystals and compressed glasses, and compared to experimental data, thereby confirming the validity of the proposed approach and assessing its limits.

3

2. Computational details

The machine learning potential for silica was developed using a neural network trained on a database of atomic configurations obtained from AIMD simulations. All AIMD simulations were carried out using the DFT code VASP with PAW pseudopotentials for O and Si atoms. We used the PBEsol exchange and correlation functional, which has been demonstrated to yield accurate structural properties for silica in relation to experimental data and an energy cutoff of 600 eV [27].

For validation of the potential and data production, the LAMMPS package [36] was used to perform MD simulations. Simulations were performed in the NVT or NPT ensemble, with a time step equal to 1 fs. The temperature was controlled by a Nose-Hoover thermostat, whose damping parameter was set to 100 fs. For NPT simulations, the pressure was controlled by a barostat with a damping parameter equal to 1000 fs.

2.1. Development of the potential

In the following, the technical details for the database generation, for the training and validity tests are given.

2.1.1. Database

To generate the training set, we conducted AIMD simulations on a 384-atom system consisting of 128 SiO_2 units in a cubic box of side 17.96285 Å at 3600 K for 9.2 ps and at 6000 K for 2.0 ps. The data at 3600K are the ones used to optimize the SHIK potential for silica [27].

To construct the database, we selected 600 snapshots at regular intervals from the two liquid trajectories, along with compressed configurations of SiO_2. These compressed configurations were obtained by reducing the size of the simulation box for some selected liquid snapshots, while scaling the atomic coordinates accordingly. We compressed the box length by 15%, 22%, 29%, 32%, 34.5%, 37%, 39%, and 42% and we included in the database the configurations taken along the relaxations of the atomic positions after compression (120 configurations in total). While the smallest volumes are highly unrealistic, they are necessary to explore the potential energy surface at very small interatomic distances. Overall, the database includes 720 configurations of 128 SiO_2 units, i.e. 276 480 atomic environments. Attempts of training the neural network with larger datasets were carried out but did not lead to drastic improvements of the RMSE.

We note that our database is much smaller and simpler than what was proposed in previous attempts for silica [31**?** –34]. In particular, we used a small number of structures and did not include any crystalline structures. In the following, we will demonstrate that this choice towards a less rich database did not impede the quality of our model.

2.1.2. Neural network training

To train the Neural Network Potential (NNP), we used the neural network-based code N2P2 and Behler-Parrinello (BP) symmetry functions for the description of the atomic environments [37]. The neural network comprises two layers of 30 neurons each and we used 39 BP radial functions and 57 BP angular functions

as descriptors [38]. For the radial functions, the values of η and r_s were set to $\{0.001, 0.01, 0.03, 0.06, 0.15, 0.3, 0.6, 1.5\}$ Å^{-2} and $\{0, 1, 2\}$ Å, respectively. For the angular functions, the values of η, λ and ζ were set to $\{0.001, 0.003, 0.007, 0.01, 0.03, 0.07, 0.2\}$ Å^{-2}, $\{-1, 1\}$ and $\{1, 4\}$, respectively. The cutoff was set to 6 Å and the activation function is a hyperbolic tangent.

The training was carried out on all energies and on 10% of the forces. The database was divided into a training set (90%) and a test set (10%). With these parameters, the lowest RMSE is 0.004 eV/atom for energy and 0.289 eV.Å^{-1} for the forces.

When comparing to previous neural network architecture and in particular to deep neural network approaches, we used a smaller number of neurons which appear to be sufficient for obtaining a highly accurate machine-learning potential.

2.1.3. Validity tests

Validation of the NNP was obtained by comparing the structure of liquid silica at 3600 K obtained from AIMD with that of two systems obtained from molecular dynamics simulations at the same temperature with the NNP: one of 384 atoms and one of 3072 atoms.

2.2. Generation of the glass samples

Silica glasses were obtained using quenches from liquids equilibrated at 3400 K and atmospheric pressure in the NPT ensemble with the LAMMPS code at zero pressure. A two-step quench procedure was used: (i) a slow quench from the liquid at 3400 K down to 1500 K during N steps and (ii) a fast quench from 1500 K down to 300 K during 100 000 steps, corresponding to a quench rate of 1.2 10^{13} K/ps. The use of this two-stage quenching protocol is justified by the fact that below 1500K, no significant relaxation takes place in our systems within the considered simulation times. Rapid quenching from this temperature onward enables us to reduce computing times without altering the quality of the final result. The values of the quench rates given hereafter correspond to the first stage. The effects of quench rate (from 3.8 10^{10} K/s to 3.8 10^{13} K/s) and of system size (from 384 to 12000 atoms) on the structural and vibrational properties of the obtained glasses were investigated. For each quench rate and size, 5 independent samples were generated and the results were averaged over the 5 samples.

Then, a 3000-atom system was used to study the effect of hydrostatic pressure at room temperature by applying a barostat to the simulation box, by steps of 2 GPa. For each step, the pressure was increased linearly during 100 ps then the system was relaxed at the target pressure in the NPT ensemble for 100 ps. Then the thermostat and barostat were released and the system was relaxed in the NVE ensemble for 100 ps during which the structural and vibrational properties were computed.

2.3. Calculations of the crystals

DFT calculations of crystalline polymorphs were performed on a primitive cell, with the PBEsol exchange and correlation functional, a plane-wave energy cutoff of 600 eV, and a convergence threshold of 0.001

eV/Å for the forces. The k-point grid used was set to 6×6×3 for cristobalite, 6×6×5 for quartz, 6×5×6 for coesite, 7×7×7 for stishovite and 1×1×2 for silicalite.

The NNP calculations of crystalline polymorphs were performed using supercells to ensure a half-length of the simulation box larger than the NNP cutoff radius (4×4×3 for cristobalite, 5×4×5 for quartz, 3×2×3 for coesite, 5×5×8 for stishovite and 1×1×1 for silicalite).

For computing the vibrational density of states (VDOS), the second order derivatives of the total energy with respect to the ions positions were calculated using a finite differences approach.

To obtain accurate phonon dispersion, VDOS DFT calculations were performed on larger supercells (2×2×2 for cristobalite, 2×2×2 for quartz, 2×1×2 for coesite, 3×3×4 for stishovite and 1×1×1 for silicalite), and the k-point grid used was set to 1×1×1. The VDOS NNP calculations were performed using the PHONON package of LAMMPS.

3. Results and discussion

The obtained NNP for silica was first tested on the structural properties of a silica liquid. Afterwards, the NNP was used to study the effects of quench rate and simulation box size on the structural and vibrational properties of amorphous silica. Finally, the transferability of the NNP was investigated on some of the most common crystalline phases of silica and on amorphous silica under pressure up to 14 GPa.

3.1. Liquids

For each system, the initial structure was obtained by randomly distribute atomic positions in a cubic box for the experimental glass density. Then the system was first minimized before being equilibrated in the NVT ensemble at 5000 K for 5 ps and then at 3600K for 0.5 ns.

First, the NNP accuracy was tested by comparing energies and forces to DFT ones on some randomly selected snapshots from the liquid trajectory at 3600K. The results presented on Fig. 1(a) and (b) for energies and forces, respectively, show an almost perfect correlation.
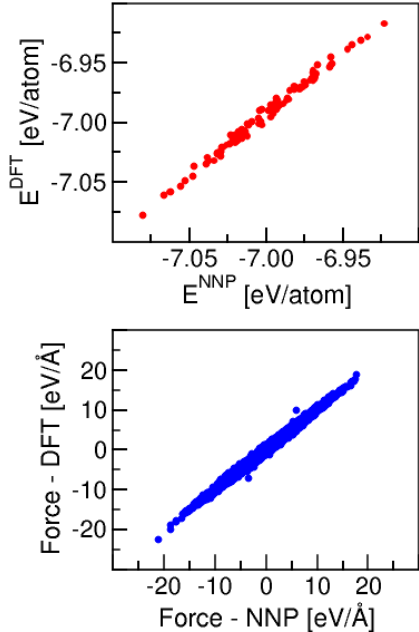

Figure 1: (a) Energies computed with the NNP vs energies computed by DFT for selected snapshots along the 3600K liquid trajectory. (b) Corresponding forces components NNP vs DFT.
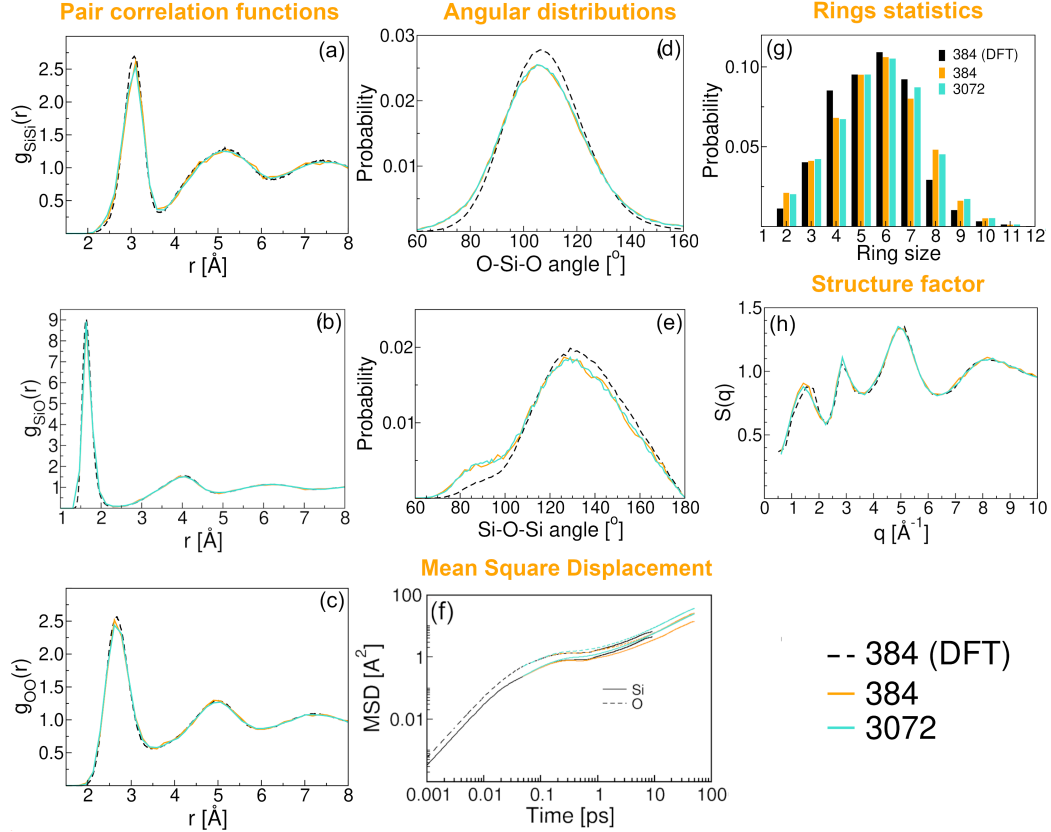
Figure 2: Characteristics of two SiO$_2$ NNP liquids of 384 and 3072 atoms at 3600 K and comparison with a 384-atom liquid obtained from AIMD: pair correlation functions (a) Si-Si, (b) Si-O, (c) O-O, angular distributions (d) O-Si-O, (e) Si-O-Si, (f) mean square displacement, (g) rings statistics, and (h) structure factor.

Snapshots were extracted from the trajectory every 5 ps to study the structural properties and compare them with the DFT reference. The pair correlation functions (PCF) and the Si-O-Si and O-Si-O bond angle distributions (BAD) were computed (Fig. 2).

The partial PCFs obtained with the NNP are in excellent agreement with the DFT reference. The results are similar for both system sizes, meaning that size effects are neg-

ligible. The partial BADs (for Si-O-Si and O-Si-O angles) present small discrepancies: The O-Si-O BAD is slightly narrower and higher in the case of DFT (Fig.2(d)) and the NNP Si-O-Si BAD exhibits a higher shoulder around 90° than the DFT one (Fig.2(e)). These discrepancies can be attributed to the presence of a larger number of defects in the NNP liquid with respect to the DFT one, including edge-sharing tetrahedra that give rise

to the shoulder at 90° in the Si-O-Si distribution.

Another important characteristic of liquid and amorphous silica is the distribution of the rings size. It has been computed using the R.I.N.G.S. code [39] with the Guttman's method and is presented in Fig. 2(g) for the three systems. The two NNP distributions are very similar, showing that there are no size effects on the structure of the liquids. However with respect to the DFT distribution, there is a larger proportion of 2-membered rings (edge-sharing tetrahedra) which is consistent with the shoulder in the Si-O-Si distribution, but also less 4-membered rings and more 8-membered rings.

Finally, the structure factors $S(q)$ of the three systems are compared in Fig.2(h). One can observe again that there are no size effects and that the agreement between the NNP liquid and the DFT one is very good.

Regarding dynamical properties, by comparing the mean square displacement (MSD) of the different liquids (Fig.2(f)), one can see a fairly good agreement between the NNP and DFT results. For the 384-atom liquid, the diffusion constants can be estimated to $\approx$ 8.0 10^{-6} cm^2/s for Si and $\approx$ 12.0 10^{-6} cm^2/s for O with DFT, and to $\approx$ 5.2 10^{-6} cm^2/s for Si and $\approx$ 9.0 10^{-6} cm^2/s for O with the NNP. For the 3072-atom system, the diffusion coefficients are $\approx$ 8.2 10^{-6} cm^2/s for Si and $\approx$ 12.8 10^{-6} cm^2/s for O with the NNP. These values are in the range of order of the values of the literature [19, 40–42]. The slower diffusion observed for the smallest system size might be due to finite size effects as reported in Ref. [43].

Overall, the structural and dynamics properties of the silica liquid obtained using the NNP are in very good agreement with that of the DFT one, validating our training.

3.2. Glasses

Following our validation of the potential on liquid properties, we will now focus on the glassy phase. We would like to raise here that our DFT database did not include any structures in this phase. Thus, such a test is certainly a challenge for NNP models which are normally considered to be poorly transferable.

3.2.1. Quench rate

Figure 3 presents the main structural and dynamical characteristics of a 384-atom SiO$_2$ glass obtained using NNP from the melt quenched at different rates ranging from 3.8×10^{13} K/s to 3.8×10^{10} K/s, and compared to that of a 384-atom glass obtained using combined classical and AIMD simulations (for details see Ref. [27]). In this procedure, the liquid equilibration and the quench are carried out using an empirical potential and the final glass structure is used as initial state for an AIMD simulation at 300 K. It has been shown that this procedure can be used to correct the deficiencies of empirical potentials in terms of local structure, but cannot be used to correct medium-range order, such as ring size distributions [10].

In Fig. 3(a), (b) and (c), the PCFs for Si-Si, Si-O and O-O are shown, respectively. The NNP Si-O and O-O PCFs look close to the DFT ones, whereas the Si-Si PCFs exhibit some discrepancies with respect to the DFT
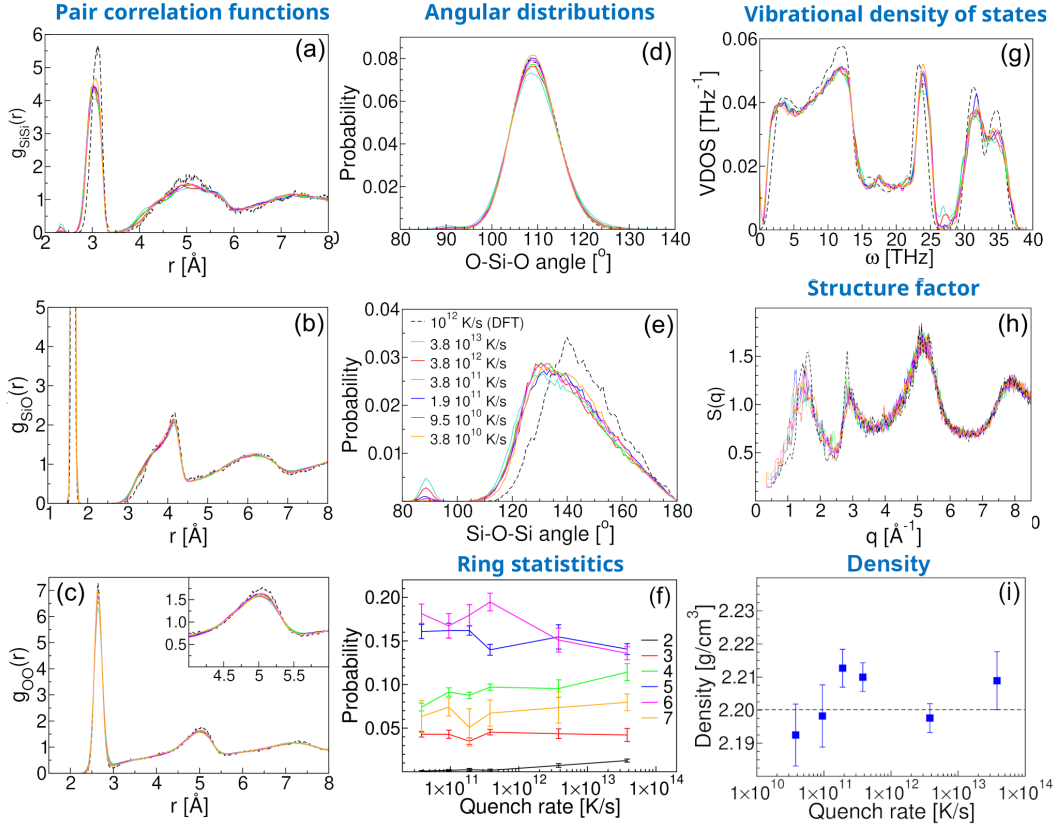
8

Figure 3: Characteristics of a 384-atom SiO$_2$ glass obtained using different quench rates: pair correlation functions (a) Si-Si, (b) Si-O, (c) O-O, angular distributions (d) O-Si-O, (e) Si-O-Si, (f) rings statistics, (g) vibrational density of states, (h) structure factor and (i) density (the dashed line corresponds to the experimental value).

ones. First, a small peak around 2.4 Å is present for the highest quench rates but is absent for the lowest quench rates and for the DFT Si-Si PCF. Second, the peak at ≈ 3.1. Å is slightly shifted towards smaller distances in NNP with respect to DFT and is smaller. This discrepancy is more pronounced the larger the quench rate. Finally, the peak around 5 Å for NNP is also different from the DFT one but does not exhibit strong quench rate effects.

Regarding the BADs (Fig. 3(d) and (e)), one can observe a slight effect of the quench rate on the O-Si-O one and a stronger effect on the Si-O-Si one. The O-Si-O BAD is slightly larger and less peaked for NNP with the highest quench rate than for DFT.

For what concerns the Si-O-Si BAD, the difference between the DFT and the NNP curves is more striking. First, there is a small

9

peak around 90° in the NNP case for almost all quench rates except the two lowest ones whereas it is absent in the DFT case. This peak corresponds to the presence of edge-sharing tetrahedra in the system. Then, the main peak maximum is located around 130° for NNP whereas it is around 140° for DFT. The position of the peak maximum slightly shifts from $\approx 126°$ to $\approx 132°$ with decreasing quench rates but this shift is not in itself sufficient to explain the difference between NNP and DFT. However there might be a residual stress in the DFT calculations since, in that case, the simulations were carried out in the NVT ensemble whereas in the NPP case, the quenches were performed in the NPT ensemble.

Figure 3(f) shows the evolution of the number of rings of different size with the quench rate. It is interesting to note that these numbers seem to converge toward a stable value for quench rates lower than $\approx 2 \times 10^{12}$ K/s. For higher quench rates, a significant evolution with the quench rate can be observe on the number of 2-membered rings (edge-sharing tetrahedra) which increases with increasing quench rate. One can also observe a concomitant increase of the 4- and 7-membered rings and a decrease of the 5- and 6-membered rings. These evolutions reflect a broadening of the ring size distribution when the quench rate increases.

The neutron structure factors for all quench rates are shown in Fig. 3(h) together with the DFT one. The quench rate effects are not significant on this quantity and the agreement with DFT is very good on the positions as well as on the height of the peaks.

The vibrational density of states (VDOS) was also computed for all quench rates (Fig. 3(g)) and compared them to the DFT one. The results show no significant quench rate effects except for the two highest ones for which the VDOS exhibits a smaller peak at 24 THz and a higher peak at 27 THz. For all other quench rates, the VDOS are in good agreement with the DFT ones. Some discrepancies can still be observed on the positions of the 24 THz and 17 THz (D_2 line) peaks and on the heights of the 12 THz band and those of the double high-frequency peak.

Finally, the densities of the glass samples at the end of the quench are shown in Fig. 3(i) for all the quench rates. All samples have a density ranging from 2.19 g/cm³ to 2.21 g/cm³, in agreement with the experimental value (2.2 g/cm³), and although density seems to increase slightly with quench rate, this trend is not significant given the error bars.

Altogether, we show that our NNP, when asked to extrapolate towards glassy systems, is able to retrieve most of the properties obtained in DFT. Furthermore, we also show that using the NNP model allows us to reach quenching rates two order of magnitude slower and to demonstrate that the quenching rate starts to affect the glassy structural properties for values larger than 10^{13} K/s.

3.2.2. System size

As for the effects of quench rate, that of the system size on the structural and vibrational properties of the obtained glass were investigated. To this aim, silica liquids of 384, 1200, 1800, 2400, 3000, 6000 and 12 000
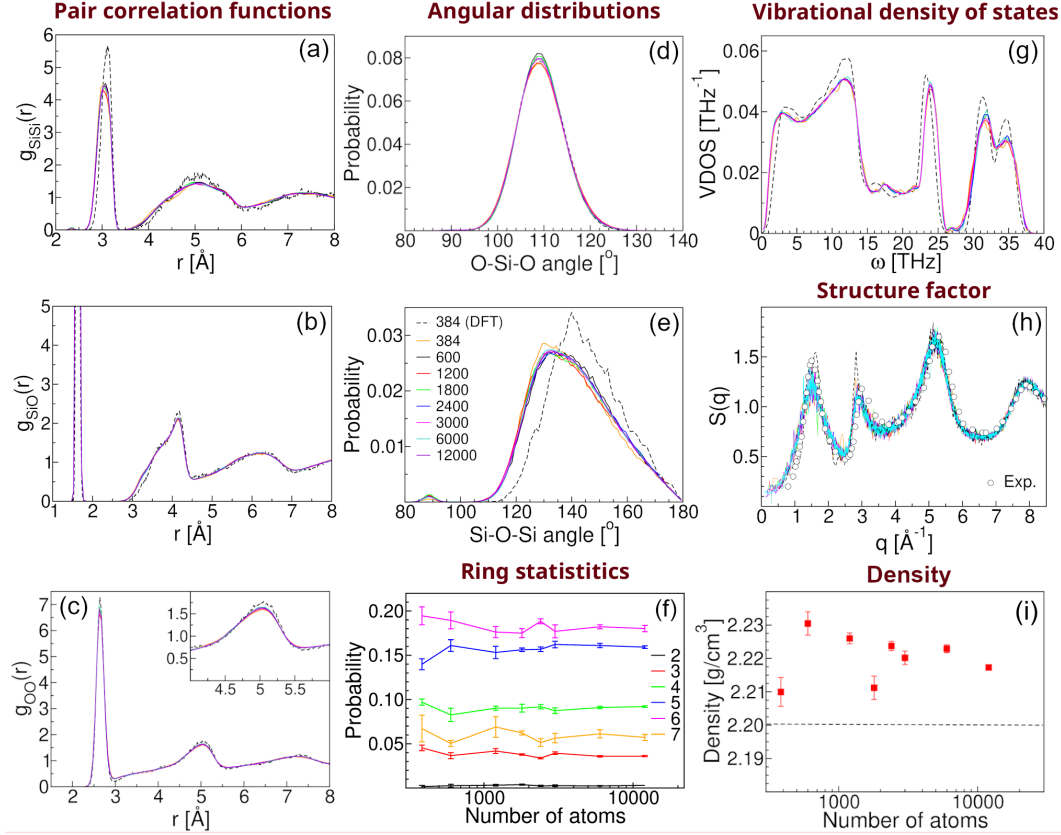
Figure 4: Characteristics of SiO$_2$ glasses of different sizes obtained using a quench rate of 3.8×10^{11} K.s^{-1}: pair correlation functions (a) Si-Si, (b) Si-O, (c) O-O, angular distributions (d) O-Si-O, (e) Si-O-Si, (f) rings statistics, (g) vibrational density of states, Experimental data from [44], (h) structure factor, experimental data from [45] and (i) density (the dashed line corresponds to the experimental value).

atoms were cooled down at a quench rate of 3.8×10^{11} K/s at which we do not observe quench rate effects anymore. For each size, five independent samples were produced and the results are obtained by averaging over the samples.

Figure 4 presents the structural and vibrational characteristics of the glasses for all investigated sizes, compared to that of the 384-atom silica glass computed using AIMD. The density of the samples (Fig. 4(i)) ranges between 2.21 g/cm^3 and 2.23 g/cm^3 which is slightly higher than the experimental density of 2.2 g/cm^3. This effect may be due to the quenching rate, which may be too high to achieve convergence of this quantity. Note, however, that there is a trend towards smaller fluctuations and convergence of the value around 2.22 with size.

However, there is no visible size effects on

the PCFs (Fig.4(a), (b) and (c)), neither on the VDOS (Fig. 4(g)) and on the the structure factors (Fig.4(h)). On the BADs (Fig. 4(d) and (e)), we can observe a few differences, but these are more related to statistics than to a size effect. The Si-O-Si BADs exhibit a small peak around 90°, evidencing the presence of edge-sharing tetrahedra in some of the glass samples. For the smallest system (384 atoms), one can observe differences on the ring size distribution (Fig.4(f)) with a larger number of 3-, 4- and 6-membered rings and less 5-membered rings than for the other sizes.

Comparison with the experimental structure factor can be found in Fig.4(h) and shows a very good agreement for what concerns the peak positions and their amplitudes. Only the second peak seems to be slightly shifted towards lower values of q but this is the case in both DFT and NNP calculations.

In Fig.4(g), the VDOS have been compared to that obtained from DFT and show very good agreement. No size effects are visible on this quantity.

In order to compare the VDOS with experiments, it is necessary to compute the *effective* VDOS which enables to connect the true vibrational density of states with that derived from inelastic neutron scattering [46]. This is obtained by computing the partial contribution coming from atoms of each species α for a given mode p:

$$g_\alpha\left(\omega_p\right) = \sum_{I=1}^{N_\alpha} \sum_{k=1}^{3} \left|\mathbf{e}_{I,k}\left(\omega_p\right)\right|^2 \qquad (1)$$

where $\mathbf{e}_{I,k}\left(\omega_p\right)$ are the 3-components of the eigenvector $\mathbf{e}(\omega_p)$ with the displacement of the particle I. The partial contribution of mode p to the effective VDOS is then:

$$g_{\text{eff}}\left(\omega_p\right) = A \sum_\alpha \frac{b_\alpha^2}{m_\alpha} g_\alpha\left(\omega_p\right) \qquad (2)$$

where

$$A = \frac{\sum_\alpha N_\alpha m_\alpha}{\sum_\alpha N_\alpha b_\alpha^2} \qquad (3)$$

with N_α, m_α and b_α are the number, mass and neutron scattering lengths (4.1491 fm for Si and 5.803 fm for O) of atoms of species α. The total effective VDOS is then:

$$G_{\text{eff}}\left(\omega\right) = \sum_{p=4}^{3N} g_{\text{eff}}\left(\omega_p\right) \delta\left(\omega - \omega_p\right) \qquad (4)$$

The effective VDOS have been computed for all sizes and the results for the 3000-atom system are compared to experiments in Fig. 5 [44, 47–49]. Note that the different experiments were done at different neutron incident energies, therefore they probe different ranges of frequencies. The computed effective VDOS show very good agreement with the experimental ones for the peak positions and amplitudes below 30 Thz. The doublet at ~32 THz and ~ 35 THz is slightly shifted to lower frequency compared to experiments but this is a well-known functional effect in the DFT calculations which is reproduced by the NNP.

Overall, the generated NNP potential gives good results compared with the ab initio data and also compared with the experimental data. The structural characteristics of
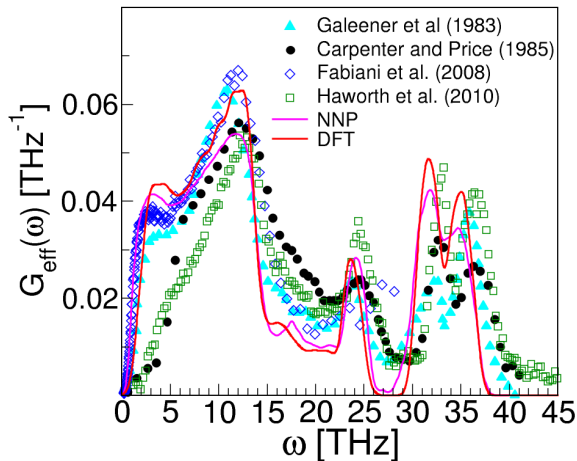
12

Figure 5: Effective neutron VDOS computed with the NNP on a 2400-atom system and compared to the one computed with DFT on a 384-atom system and to experiments from [44, 47–49].

the glasses obtained by the slowest quenching are comparable to those obtained with the best potentials in literature [21, 27] and with those obtained using the most recent machine learning potentials [31, 32, 34]. What is more remarkable is the excellent reproduction of the vibrational data obtained with this potential. No 'classical' empirical potential has so far been able to provide a good VDOS. Only machine learning potentials such as this one or the NNP of Li and Ando [31] have been able to do so.

3.3. Transferability of the potential

The results obtained on the structural and dynamic properties of liquids and glasses demonstrate that the NNP potential is sufficiently accurate to reproduce these characteristics at the same DFT level as that used to build the training database. Since the configurations stored in the database represent snapshots of liquids at elevated temperatures, it is reasonable to expect that the adjusted potential would provide a suitable description for both liquids and amorphous materials. It is therefore interesting to check whether such a potential is capable of correctly describing structures further away from those included in the fitting process, such as the crystalline polymorphs of silica. Another valuable assessment of its transferability involves subjecting the glasses to compression and analyzing their response to pressure.

3.3.1. Crystals

Structural properties. The transferability of the NNP was tested on systems not included in the training database : α-cristobalite, α-quartz, coesite, stishovite and silicalite silica crystals. The structures of each polymorph were relaxed using the NNP, and compared to DFT minimizations. During the relaxations, the atomic positions, the volume and the shape of the simulation cells were allowed to change. The errors made by the NNP model with respect to the DFT reference are shown in Fig. 6 for lattice parameters, average Si-O bond lengths and average Si-O-Si angles for all relaxed structures. Overall, we obtain good results, especially for quartz and coesite whose relative errors with respect to the DFT are lower than 1%. However, the results are less good for the stishovite, with a relative error exceeding 5% for two of the lattice parameters. The basic structural unit of stishovite being an octahedron SiO_6, unlike other silica polymorphs in which silicon adopts a tetra-

13

hedral coordination geometry, we can assume that the NNP is not able to reproduce a perfect octahedral arrangement. This might be due to the fact that the database contains mainly 4-fold coordinated Si atoms, even if a non negligible proportion of 5- and 6-fold coordinated Si atoms might be present in the AIMD liquid at high temperature.
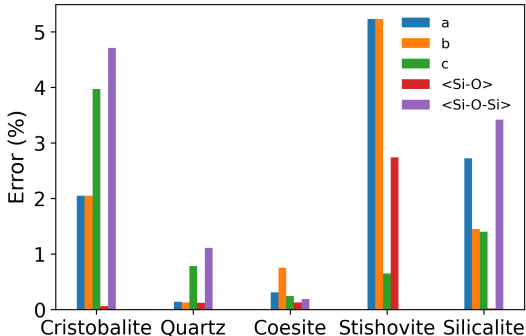

Figure 6: Errors made by the NNP model for the prediction of the lattice parameters, average Si-O bond lengths and average Si-O-Si angles of each relaxed structure, relative to the DFT reference values for silica polymorphs: α-cristobalite, α-quartz, coesite, stishovite, and silicalite.

The volume of each relaxed crystal structure was calculated : errors made by the NNP relative to the DFT are respectively equal to 7.81% , 0.97%, 0.28%, 9.91% and 5.41% for α-cristobalite, α-quartz, coesite, stishovite and silicalite. The ML potential developed by Erhard *et al.* [34] gives much better results, with errors not exceeding 0.6% for the volume of these same structures. Other structural and elastic properties of theses polymorphs are also predicted with excellent accuracy, but this is consistent with the fact that they in-

cluded crystalline structures in the reference database.

Vibrational properties. The vibrational density of states (VDOS) were computed for each relaxed crystal structure, and compared to the DFT ones (Fig. 7). The results observed are similar to those obtained for the lattice parameters : the agreement with DFT is good, except for the stishovite whose properties are once again not accurately reproduced by the NNP. This is consistent with the assumption that the NNP is not able to reproduce octahedral silica-based systems. For all other silica polymorphs, we can note that the position and the height of the double high-frequency peak are reproduced with very good accuracy.

The 24 THz peaks are also in good agreement with the DFT ones, especially for quartz and coesite. For the lower frequencies, some discrepancies can be observed on the position and the height of the peaks, particularly for cristobalite and quartz.
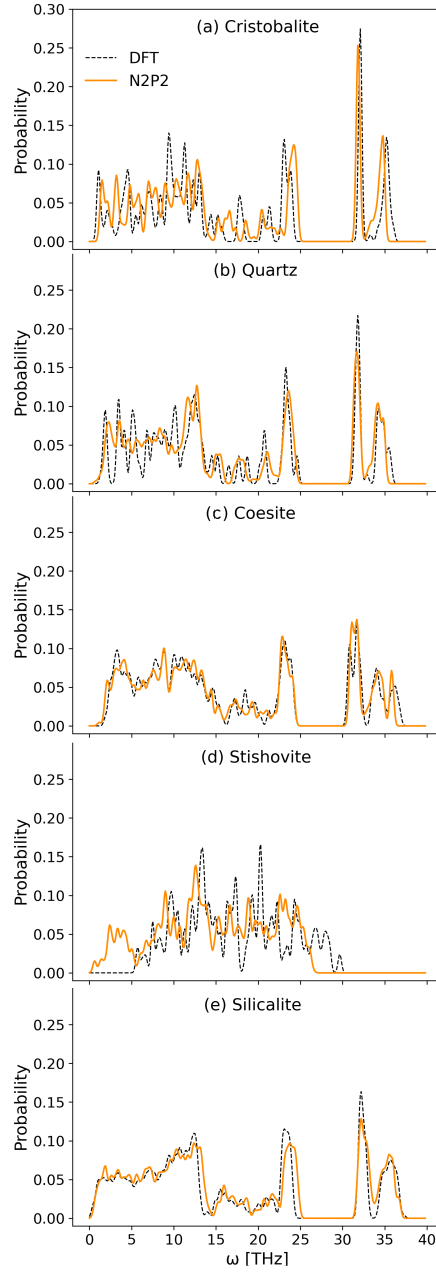
Figure 7: Comparison of vibrational density of states (VDOS) between DFT and NNP, for (a) α-cristobalite, (b) α-quartz, (c) coesite, (d) stishovite, and (e) silicalite silica polymorphs.

3.3.2. Glasses under pressure

The structural and dynamic properties of silica glasses are well reproduced compared to DFT and behave correctly with respect to simulation parameters such as quenching rate and simulation box size. Therefore, it is interesting to test the transferability limits of such a potential by examining how it behaves when the glass is subjected to pressure. For this purpose, we chose to apply hydrostatic pressure in steps of 2 GPa from 0 to 14 GPa to the 3000-atom glass samples obtained at 300K using a $3.8 \ 10^{11}$ K/s quench rate.

The obtained results are presented in Fig. 8. First of all, the Si-O bond length appears to be quite resistant to pressure changes up to 14 GPa and only the second peak of the Si-O PCF is slightly affected by pressure (Fig.8(b)). In contrast, the first and second peaks of the Si-Si PCFs (Fig. 8(a)) exhibit notable shifts in position and intensity, as well as the second peak in the O-O PCFs (Fig. 8(c)), indicating that isostatic pressure primarily influences the interconnection of SiO_4 tetrahedra. This effect is particularly pronounced in the Si-Si PCF, where all the peaks experience a significant shift towards shorter distances under pressure. This observation is closely associated with the changing Si-O-Si angles (Fig. 8(e)), which gradually decrease as compression is applied, causing the tetrahedra to come closer together whereas the tetrahedral angle O-Si-O peak is not shifted but only enlarged (Fig. 8(d)). Note moreover that the proportion of defects such as edge-sharing tetrahedra increases with pressure. The evo-

lution of 4- and 5-fold coordinated Si atoms (resp. Si_4 and Si_5) and of 3-fold coordinated O atoms (O_3) as a function of pressure are depicted in Fig. 9. From 8 GPa, one can observe the occurrence of Si_5 and O_3 which proportion increases to $\sim$ 6 % and $\sim$ 3 %, respectively at 14 GPa. This is in very good agreement with recent experiments [50, 51] and with previous molecular dynamics simulations [27, 52]. However our results differ strongly from those of Ref. [35] which found almost 100 % of Si_5 at 9 GPa and important finite size effects on their systems subject to pressure.

Figure 8(f) presents the evolution of the rings size with pressure. Up to 8 GPa, no noticeable change can be observed. At higher pressure, the proportion of 2-, 3-, 4- and 5-membered rings increases substantially whereas that of the 6-membered rings remains constant and the number of 7-membered rings decreases. This result is consistent with the emergence of defects in the connectivity of the tetrahedra as suggested by the evolution of the angular distributions with pressure.

In summary, the connectivity between the tetrahedra evolves towards smaller angles and we observe the apparition of smaller rings, and of 5-fold coordinated Si atoms and 3-fold coordinated O atoms from 8 GPa.

This leads to an evolution of the medium-range order with pressure that is better seen on the structure factor S(q) in Fig. 8(h): the first peak (First Sharp Diffraction Peak, FSDP) is shifted towards larger q-vector and its intensity decreases. This evolution of the FSDP with pressure is experimentally ob-
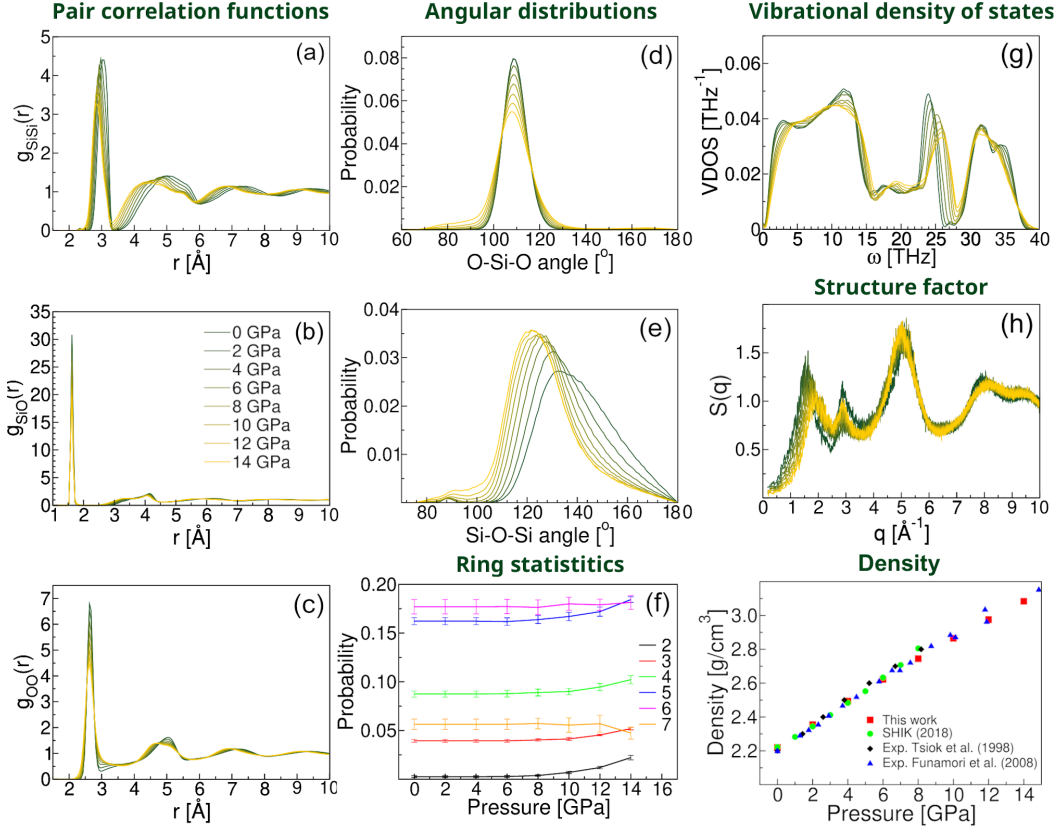
16

Figure 8: Characteristics of a 3000-atom SiO$_2$ glass obtained using a quench rate of 3.8 10^{11} K.s^{-1} at different pressures: pair correlation functions (a) Si-Si, (b) Si-O, (c) O-O, angular distributions (d) O-Si-O, (e) Si-O-Si, (f) rings statistics, (g) vibrational density of states, (h) structure factor and (i) density.

served and its position as a function of pressure has been measured [51, 53–56]. It is depicted in Fig. 10 together with the position of the FDSP obtained using the NNP. The agreement is particularly good with most of the experimental data. Some discrepancies can be observed in particular with the open squares extracted from the publication of Inamura *et al.* in 2004. However these points correspond to data acquired over long times, during which the samples heated up, causing

the FSDP to drift [53].

The VDOS were computed at the different investigated pressures (Fig. 8(g)) and exhibit significant modifications under compression: (i) the peak around 3 THz shifts towards higher frequency and the one arund 11 THz towards lower frequency inducing a flattening of the main low frequency band, (ii) the 17 THz and 24 Thz peaks are shifted towards higher frequencies and (ii) the high-frequency double-peak merges into a single
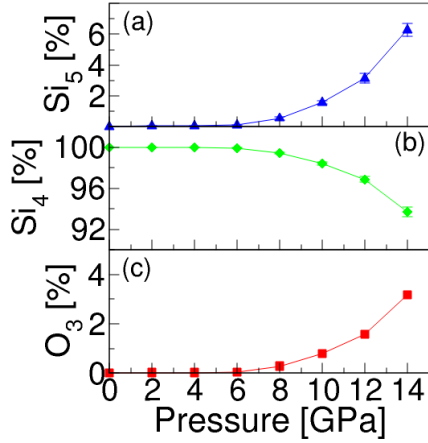
Figure 9: Evolution of the percentage of (a) 5-fold coordinated Si atoms (Si_5), (b) 4-fold coordinated Si atoms (Si_4) and (c) 3-fold coordinated O atoms (O_3) as a function of pressure.

Figure 10: Pressure dependence of the FSDP position (red circles) compared to data extracted from the literature [51, 53–56].

peak. The evolution of the 11 THz, 17 THz and 24 Thz peaks as a function of pressure are depicted in Fig. 11. The peak around 11 THz is attributed mainly to vibrational modes involving oxygen atoms (it is different from the breathing mode of the 4-membered rings around 15 THz which is only visible in the Raman spectra) [57]. Those modes are related to large rings that become less stiff with pressure (Fig. 11(a)). The 17 THz peak is attributed to the breathing modes of 3-membered rings (D_2 line) which experimental frequency is around 18 THz. Upon compression these modes are shifted to higher frequencies corresponding to a stiffening of the rings, and then seem to saturate to a value of $\approx$ 19.5 THz from 10 GPa (Fig. 11(b)). The D_2 line shift to higher frequency under pressure has already been observed experimentally [57, 58] and theoretically in *ab initio*
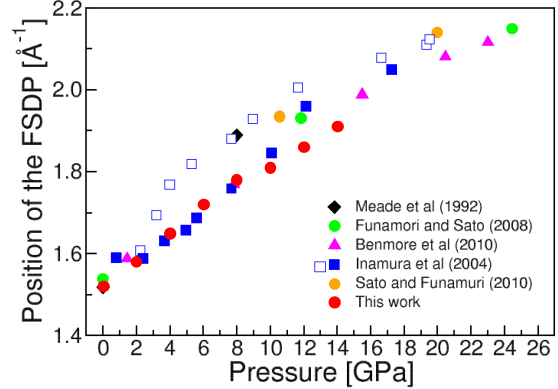
simulations[9, 59]. The band at 24 THz corresponds to bending of the Si-O-Si angle in the plane [11]. Its evolution is similar to that of the D_2 line with an increase up to 10 GPa followed by a stagnation (Fig. 11(c)).

Finally, one important feature of silica is the evolution of its density upon isostatic compression. Figure 8(i) shows this evolution as obtained with the NNP potential and compared with experimental results [54]. The agreement is very good showing the validity of our potential on this range of pressures.

4. Conclusion

Using AIMD trajectories of liquid silica at high temperature and pressure, we built a database composed of a limited number of configurations that was used to train a neural network interatomic potential with Behler-Parrinello descriptors. This potential was
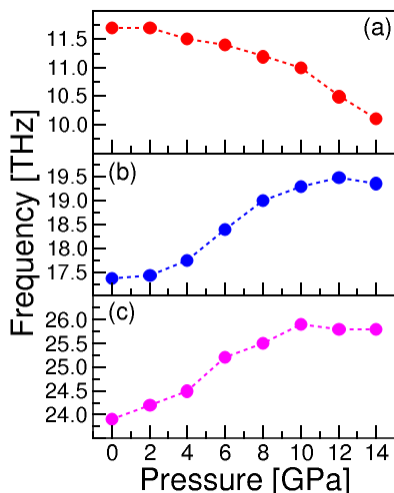
Figure 11: Evolution of the frequency peak around ≈ 11 THz (a), ≈ 17 THz (b) and ≈ 24 THz (c) as a function of isostatic pressure.

first validated by performing MD simulations for liquid silica and for two different sizes. The structural and dynamic properties were in agreement with the DFT results, with the caveat of a slightly too high edge sharing number in NNP. Afterwards, the NNP was used to generate silica glass samples while testing parameters such as the quench rate and the system size. If the latter seems to have little impact on the structural and vibrational properties of the glass, except for the smallest size, a too high quench rate ($\gtrsim 10^{12}$ K/s) induces structural defects such as edge-sharing tetrahedra and a modification of the medium-range order.

The transferability of NNP was then tested on crystals, on the one hand, and on glass under isostatic pressure, on the other. In the former case, lattice parameters and struc-tural features were obtained with less than 5% error from DFT, with surprisingly good agreement for quartz and coesite. As far as vibrational properties are concerned, the main features of the vibrational spectra were found with very good agreement for peak positions and amplitudes for quartz and coesite, while slight shifts are observed in the spectra of cristobalite and silicalite. In the case of stishovite, the main band is shifted and agreement with DFT is poor, which can be attributed to the fact that the database does not contain data on perfect octahedral order, even if a non negligible proportion of 5- and 6-fold coordinated Si atoms might be present in the AIMD liquid at high temperature. Over-all, the NNP gives surprisingly good results for silica crystals, given that none of these structures were included in the database. In Ref. [60], the authors also explored the ex-tent to which a database consisting exclu-sively of liquid configurations would be suf-ficient to develop a NN potential transferable to crystalline structures. Their conclusions are very similar to ours, and they also show that including data from very high-pressure liquids could improve transferability. In ad-dition, including the crystalline structures in the database will more likely improve the agreement with DFT.

For glass under isostatic pressure, agree-ment with the DFT is very good up to 14 GPa, and also satisfactory compared with ex-perimental results. NNP exhibits good struc-tural and vibrational properties, which leads us to believe that it could be successfully used for applications such as indentation and frac-ture studies, once its ability to reproduce me-

19

chanical properties has been verified.

We have proposed an approach able to generate a very good quality potential for describing silica liquid and glass. Our aim was not to provide a potential that can be transferred to all silica phases, but rather to demonstrate that the use of a well-chosen database and a not-too-big neural network can be sufficient to provide a potential suited to a specific study. This approach may be of interest for methods such as active learning, where the potential is readjusted during dynamics when the NNP forces deviate too far from the DFT reference or for multi-scale simulations, such as in the work of Wakabayashi et al. [61]. It is also a step in line with the desire to move towards frugal artificial intelligence, enabling the use of fewer resources for an equivalent result. In this direction, it is possible to further reduce the computational cost by generating molecular dynamics trajectories using a classical potential, from which only the configurations included in the database are calculated at an *ab initio* level. The importance of this search for efficient and less computationally demanding machine learning is reflected in current developments, such as those aimed at generating potentials from equivariant graph neural networks [62, 63]. *Note added in proof.* Note that during the achievement of this work, Kobayashi *et al.* have published results in line with the output of the present paper[64].

5. Acknowledgments

6. Data availability

The data required to reproduce these findings can be shared upon reasonable request.

References

[1] I. W. Donald, Waste immobilization in glass and ceramic based hosts: Radioactive, toxic and hazardous wastes, Wiley Online Library (2010). doi:10.1002/9781444319354.

[2] T. C. Keller, S. Isabettini, D. Verboekend, E. G. Rodrigues, J. Pérez-Ramírez, Hierarchical high-silica zeolites as superior base catalysts, Chem. Sci. 5 (2014) 677–684. doi:10.1039/C3SC51937F.

[3] D. Neuville, C. Le Losq, Link between medium and long-range order to macroscopics properties of silicate glasses and melts, Reviews in Mineralogy and Geochemistry 87 (2022) 105–162.

[4] R. Howie, Silica: Physical behavior, geochemistry and materials applications., Mineralogical Magazine 60 (1996) 390–391. doi:10.1180/minmag.1996.060.399.16.

[5] W. Kob, S. Ispas, First-principles simulations of glass-formers, Encyclopedia of Glass Science, Technology, History, and Culture 1 (2021) 233–243.

[6] H. Liu, Z. Zhao, Q. Zhou, R. Chen, K. Yang, Z. Wang, L. Lang, M. Bauchy, Challenges and opportunities in atomistic simulations of glasses: a review 354 (2022) 35–78.

[7] J. Du, A. Cormack, Atomistic simulations of glasses: Fundamentals and applications (2022).

[8] J. Sarnthein, A. Pasquarello, R. Car, Origin of the high-frequency doublet in the vibrational spectrum of vitreous sio2, Science 275 (5308) (1997) 1925–1927.

[9] R. C. A. Pasquarello, Identification of raman defect lines as signatures of ring structures in vitreous silica, Phys. Rev. Lett. 80 (1998) 5145.

[10] M. Benoit, S. Ispas, P. Jund, R. Jullien, Model of silica glass from combined classical and ab initio molecular-dynamics simulations, Eur. Phys. J. B 13 (2000) 631–636.

[11] P. Umari, A. Pasquarello, First-principles analysis of the raman spectrum of vitreous silica: comparison with the vibrational density of states, Journal of Physics: Condensed Matter 15 (16) (2003) S1547. doi:10.1088/0953-8984/15/16/304.

[12] A. Pasquarello, J. Sarnthein, R. Car, Dynamic structure factor of vitreous silica from first principles: Comparison to neutron-inelastic-scattering experiments, Phys. Rev. B 57 (1998) 14133.

[13] B. W. H. van Beest, G. J. Kramer, R. A. van Santen, Force fields for silicas and aluminophosphates based on ab initio calculations, Phys. Rev. Lett. 64 (1990) 1955–1958. doi:10.1103/PhysRevLett.64.1955.

[14] S. Tsuneyuki, M. Tsukada, H. Aoki, Y. Matsui, First-principles interatomic potential of silica applied to molecular dynamics, Phys. Rev. Lett. 61 (1988) 869–872. doi:10.1103/PhysRevLett.61.869.

[15] A. Pedone, G. Malavasi, M. C. Menziani, A. N. Cormack, U. Segre, A new self-consistent empirical interatomic potential model for oxides, silicates, and silica-based glasses, J. Phys. Chem. B 110 (2006) 11780–11795.

[16] A. C. Van Duin, A. Strachan, S. Stewman, Q. Zhang, X. Xu, W. A. Goddard, Reaxffsio reactive force field for silicon and silicon oxide systems, J. Phys. Chem. A 107 (2003) 3803–3811.

[17] B. Feuston, S. Garofalini, Empirical three-body potential for vitreous silica, J. Chem. Phys. 89 (1988) 5818–5824. doi:10.1063/1.455531.

[18] P. Tangney, S. Scandolo, An ab initio parametrized interatomic force field for silica, J. Chem. Phys 117 (2002) 8898–8904. doi:10.1063/1.1513312.

[19] A. Carre, J. Horbach, S. Ispas, W. Kob, New fitting scheme to obtain effective potential from car-parrinello molecular-dynamics simulations: Application to silica, Europhysics Letters 82 (2008) 17001.

[20] Y. Yu, B. Wang, M. Wang, G. Sant, M. Bauchy, Revisiting silica with reaxff: Towards improved predictions of glass structure and properties via reactive molecular dynamics, Journal of Non-Crystalline Solids 443 (2016) 148–154.

[21] A. Pedone, M. Bertani, L. Brugnoli, A. Pallini, Interatomic potentials for oxide glasses: Past, present, and future, Journal of Non-Crystalline Solids: X 15 (2022) 100115. doi:10.1016/j.nocx.2022.100115.

[22] S. Urata, Y. Takato, K. Maeda, Molecular dynamics investigation of the fracture mechanism of a glass-ceramic containing cleavable crystals, J. Am. Ceram. Soc. 102 (2019) 5138–5148. doi:10.1111/jace.16399.

[23] Z. Zhang, S. Ispas, W. Kob, Origin of the non-linear elastic behavior of silicate glasses, Acta Mater. 231 (2022) 117855. doi:10.1016/j.actamat.2022.117855.

[24] X. Zhang, B. B. Laird, H. Liang, W. Lu, Z. Yu, X. Ma, Y. Cheng, Y. Yang, Atomistic characterization of the SiO2 high-density liquid/low-density liquid interface, J. Chem. Phys. 157 (2022) 134703. doi:10.1063/5.0107674.

[25] T. Du, S. S. Sørensen, T. To, M. M. Smedskjaer, Oxide glasses under pressure: Recent insights from experiments and simulations, Journal of Applied Physics 131 (2022) 170901. doi:10.1063/5.0088606.

[26] A. Tirelli, K. Nakano, Topological data analysis for revealing the structural origin of density anomalies in silica glass, J. Phys. Chem. B 127 (2023) 3302–3311, pMID: 36999959. doi:10.1021/acs.jpcb.2c09009.

[27] S. Sundararaman, L. Huang, S. Ispas, W. Kob, New optimization scheme to obtain interaction potentials for oxide glasses, J. Chem. Phys. 148 (2018) 194504. doi:10.1063/1.5023707.

[28] S. Sundararaman, L. Huang, S. Ispas, W. Kob, New interaction potentials for alkali and alkaline-earth aluminosilicate glasses, J. Chem. Phys. 150 (2019) 154505. doi:10.1063/1.5079663.

[29] S. Sundararaman, L. Huang, S. Ispas, W. Kob, New interaction potentials for borate glasses with mixed network formers, J. Chem. Phys. (2020) 104501doi:10.1063/1.5142605.

[30] M. Bertani, M. C. Menziani, A. Pedone, Improved empirical force field for

multicomponent oxide glasses and crystals, Phys. Rev. Mater. 5 (2021) 045602. doi:10.1103/PhysRevMaterials.5.045602.

[31] W. Li, Y. Ando, Comparison of different machine learning models for the prediction of forces in copper and silicon dioxide, Phys. Chem. Chem. Phys. 20 (2018) 30006–30020. doi:10.1039/C8CP04508A.

[32] I. A. Balyakin, S. V. Rempel, R. E. Ryltsev, A. A. Rempel, Deep machine learning interatomic potential for liquid silica, Phys. Rev. E 102 (2020) 052125. doi:10.1103/PhysRevE.102.052125.

[33] M. Wang, N. Anoop Krishnan, B. Wang, M. Smedskjaer, J. Mauro, M. Bauchy, A new transferable interatomic potential for molecular dynamics simulations of borosilicate glasses, J. Non-Cryst. Solids 498 (2018) 294–304. doi:10.1016/j.jnoncrysol.2018.04.063.

[34] L. C. Erhard, J. Rohrer, K. Albe, V. L. Deringer, A machine-learned interatomic potential for silica and its relation to empirical models, npj Comput Mater 8 (2022).

[35] Y. Qi, X. Guo, H. Wang, S. Zhang1, M. Li, P. Zhou, D. Guot, Reversible densification and cooperative atomic movement induced "compaction" in vitreous silica: a new sight from deep neural network interatomic potentials., J Mater Sci 58 (2023). doi:10.1007/s10853-023-08599-w.

[36] A. P. Thompson, H. M. Aktulga, R. Berger, D. S. Bolintineanu, W. M. Brown, P. S. Crozier, P. J. in 't Veld, A. Kohlmeyer, S. G. Moore, T. D. Nguyen, R. Shan, M. J. Stevens, J. Tranchida, C. Trott, S. J. Plimpton, LAMMPS - a flexible simulation tool for particle-based materials modeling at the atomic, meso, and continuum scales, Comp. Phys. Comm. 271 (2022) 108171. doi:10.1016/j.cpc.2021.108171.

[37] A. Singraber, T. Morawietz, J. Behler, C. Dellago, Parallel multistream training of high-dimensional neural network potentials, Journal of Chemical Theory and Computation 15 (5) (2019) 3075–3092. doi:10.1021/acs.jctc.8b01092.

[38] J. Behler, M. Parrinello, Phys. Rev. Lett. 98 (2007) 146401.

[39] S. Le Roux, P. Jund, Ring statistics analysis of topological networks: New approach and application to amorphous ges2 and sio2 systems, Computational Materials Science 49 (2010) 70–83. doi:10.1016/j.commatsci.2010.04.023.

[40] B. B. Karki, D. Bhattarai, L. Stixrude, First-principles simulations of liquid silica: Structural and dynamical behavior at high pressure, Phys. Rev. B 76 (2007) 104205. doi:10.1103/PhysRevB.76.104205.

[41] A. Takada, R. G. Bell, C. R. A. Catlow, Molecular dynamics study of liquid silica under high pressure,

Journal of Non-Crystalline Solids 451 (2016) 124–130, structure, dynamics and applications of non-crystalline solids and disordered materials. doi:10.1016/j.jnoncrysol.2016.06.005.

[42] T. F. Soules, G. H. Gilmer, M. J. Matthews, J. S. Stolken, M. D. Feit, Silica molecular dynamic force fields—a practical assessment, Journal of Non-Crystalline Solids 357 (6) (2011) 1564–1573. doi:10.1016/j.jnoncrysol.2011.01.009.

[43] A. T. Celebi, S. H. Jamali, A. Bardow, T. J. H. Vlugt, O. A. Moultos, Finite-size effects of diffusion coefficients computed from molecular dynamics: a review of what we have learned so far, Molecular Simulation 47 (10-11) (2021) 831–845. doi:10.1080/08927022.2020.1810685.

[44] F. Galeener, A. Leadbetter, M. Stringfellow, Phys. Rev. B 27 (1983) 1052.

[45] S. Susman, K. J. Volin, D. L. Price, M. Grimsditch, J. P. Rino, R. K. Kalia, P. Vashishta, G. Gwanmesia, Y. Wang, R. C. Liebermann, Intermediate-range order in permanently densified vitreous sio_2: A neutron-diffraction and molecular-dynamics study, Phys. Rev. B 43 (1991) 1194–1197. doi:10.1103/PhysRevB.43.1194.

[46] S. N. Taraskin, S. R. Elliott, Connection between the true vibrational density of states and that derived from inelastic neutron scattering, Phys. Rev. B 55 (1997) 117–123. doi:10.1103/PhysRevB.55.117.

[47] J. M. Carpenter, D. L. Price, Correlated motions in glasses studied by coherent inelastic neutron scattering, Phys. Rev. Lett. 54 (1985) 441–443. doi:10.1103/PhysRevLett.54.441.

[48] E. Fabiani, A. Fontana, U. Buchenau, Neutron scattering study of the vibrations in vitreous silica and germania, The Journal of Chemical Physics 128 (24) (2008) 244507. doi:10.1063/1.2937731.

[49] R. Haworth, G. Mountjoy, M. Corno, P. Ugliengo, R. J. Newport, Probing vibrational modes in silica glass using inelastic neutron scattering with mass contrast, Phys. Rev. B 81 (2010) 060301. doi:10.1103/PhysRevB.81.060301.

[50] A. Zeidler, K. Wezka, R. F. Rowlands, D. A. J. Whittaker, P. S. Salmon, A. Polidori, J. W. E. Drewitt, S. Klotz, H. E. Fischer, M. C. Wilding, C. L. Bull, M. G. Tucker, M. Wilson, High-pressure transformation of sio_2 glass from a tetrahedral to an octahedral network: A joint approach using neutron diffraction and molecular dynamics, Phys. Rev. Lett. 113 (2014) 135501. doi:10.1103/PhysRevLett.113.135501.

[51] C. Meade, R. J. Hemley, H. K. Mao, High-pressure x-ray diffraction of sio_2

glass, Phys. Rev. Lett. 69 (1992) 1387–1390. doi:10.1103/PhysRevLett.69.1387.

[52] Y. Liang, C. R. Miranda, S. Scandolo, Mechanical strength and coordination defects in compressed silica glass: Molecular dynamics simulations, Phys. Rev. B 75 (2007) 024205. doi:10.1103/PhysRevB.75.024205.

[53] Y. Inamura, Y. Katayama, W. Utsumi, K.-i. Funakoshi, Transformations in the intermediate-range structure of sio_2 glass under high pressure and temperature, Phys. Rev. Lett. 93 (2004) 015501. doi:10.1103/PhysRevLett.93.015501.

[54] N. Funamori, T. Sato, A cubic boron nitride gasket for diamond-anvil experiments, Rev Sci Instrum 79 (2008) 053903.

[55] T. Sato, N. Funamori, High-pressure structural transformation of sio_2 glass up to 100 gpa, Phys. Rev. B 82 (2010) 184102. doi:10.1103/PhysRevB.82.184102.

[56] C. J. Benmore, E. Soignard, S. A. Amin, M. Guthrie, S. D. Shastri, P. L. Lee, J. L. Yarger, Structural and topological changes in silica glass at pressure, Phys. Rev. B 81 (2010) 054105. doi:10.1103/PhysRevB.81.054105.

[57] K. J. K. Russell J. Hemley, Charles T. Prewitt, High-pressure behavior of silica, Reviews in Mineralogy and Geochemistry 29 (1994) 41.

[58] C. Martinet, A. Kassir-Bodon, T. Deschamps, A. Cornet, S. L. Floch, V. Martinez, B. Champagnon, Permanently densified sio2 glasses: a structural approach, Journal of Physics: Condensed Matter 27 (32) (2015) 325401. doi:10.1088/0953-8984/27/32/325401.

[59] A. Rahmani, M. Benoit, C. Benoit, Signature of small rings in the raman spectra of normal and compressed amorphous silica: A combined classical and ab initio study, Phys. Rev. B 68 (2003) 184202. doi:10.1103/PhysRevB.68.184202.

[60] I. Balyakin, N. Ryltsev, R.E. Chtchelkatchev, Liquid–crystal structure inheritance in machine learning potentials for network-forming systems, Jetp Lett. 117 (2023) 370–376. doi:doi.org/10.1134/S0021364023600234.

[61] D. Wakabayashi, K. Shimamura, A. Koura, F. Shimojo, Large-scale molecular-dynamics simulations of sio2 melt under high pressure with robust machine-learning interatomic potentials, Journal of the Physical Society of Japan 92 (7) (2023) 074002. doi:10.7566/JPSJ.92.074002.

[62] C. Park, M. Kornbluth, J. Vandermause, C. Wolverton, B. Kozinzky, J. Mailoa, Accurate and scalable graph neural network force field and molecular dynamics with direct force architecture, npj Comput Mater 7 (2021). doi:10.1038/s41524-021-00543-3.

[63] S. Batzner, A. Musaelian, L. Sun, M. Geiger, J. Mailoa, M. Kornbluth, N. Molinari, S. T.E., B. Kozinsky, E(3)-equivariant graph neural networks for data-efficient and accurate interatomic potentials, Nat Commun. 3(1) (2022). doi:10.1038/s41467-022-29939-5.

[64] K. Kobayashi, M. Okumura, H. Naka-mura, M. Itakura, M. Machida, S. Urata, K. Suzuya, Machine learning molecular dynamics reveals the structural origin of the first sharp diffraction peak in high-density silica glasses., Sci Rep 13 (2023) 18721. doi:10.1038/s41598-023-44732-0.